PAPER • **OPEN ACCESS**

Green synthesis of ZnO nanoparticles for DSSC photoanode: a joint experimental and density functional theory study

To cite this article: Stephen Balabye *et al* 2025 *Mater. Res. Express* **12** 105004

Materials Research Express

OPEN ACCESS

RECEIVED
10 July 2025

REVISED
30 August 2025

ACCEPTED FOR PUBLICATION
29 September 2025

PUBLISHED
8 October 2025

PAPER

Green synthesis of ZnO nanoparticles for DSSC photoanode: a joint experimental and density functional theory study

Stephen Balabye[1], **Emmanuel Mushebo**[1], **Stella Nasejje**[1], **Egor Moses**[2] **and Emma Panzi Mukhokosi**[1,*]

[1] Department of Physics, Faculty of Science, Kyambogo University, PO Box 1, Kyambogo, Uganda
[2] Department of Chemistry, Faculty of Science and Education, Busitema University, PO Box 236, Tororo, Uganda
[*] Author to whom any correspondence should be addressed.

E-mail: epmukhokosi@kyu.ac.ug

Keywords: ZnO, DSSC, DFT, green synthesis

Abstract

Green synthesis, a biological method for nanoparticle preparation, has been suggested as a possible eco-friendly alternative to chemical and physical methods. In this study, we report on first principles calculations and the green synthesis of zinc oxide (ZnO) nanoparticles (NPs) from *Erythrina abyssinica* stem bark extract calcined under different temperatures (300 – 700 °C) for application as a photoanode in dye sensitized solar cells (DSSCs). Synthesized ZnO NPs were subjected to characterization using x-ray diffraction, Scanning Electron Microscopy, Energy Dispersive X-Ray spectroscopy, Ultraviolet–Visible spectroscopy and photoluminescence analysis. The analysis revealed that highly crystalline hexagonal ZnO NPs were formed at 700 °C, with the nanospheres agglomeration into non-uniform distinct NPs with a band gap energy of 3.12 eV. The DSSC exhibited a short circuit current density (J_{sc}) of 56 μA cm^{-2}, open circuit voltage (V_{oc}) of 161 mV, a fill factor of 0.265, and a power conversion efficiency of 0.0024% using 100 mWcm^{-2} illumination. Density Functional Theory (DFT) calculations were performed on the structural, electronic, and dielectric properties of ZnO at the atomic level. The Projected Density of States (PDOS) analysis revealed that Zn-4s and O-2p orbitals contributed significantly to the conduction band minimum (CBM) and valence band maximum (VBM), respectively, and a direct band gap at Gamma in the electronic band structure. Dielectric function analysis revealed anisotropy in the refractive index and dielectric function, with noticeable transparency in the visible spectrum and strong absorption in the ultraviolet, making them potential candidates in a set of photoelectrochemical applications.

1. Introduction

A lifestyle centered on power-consuming devices and machinery is a notable aspect of modern society. Various materials are needed for this continued modernization in society, and these should preferably be sustainable for different applications [1]. According to the International Energy Outlook study (2021), the anticipated energy consumption of more than eight billion people globally is currently over 13 terawatts (TW) and is predicted to rise by 10 TW by 2050. Fossil fuels are well known for being an unsustainable energy source due to their quick depletion and generation of pollutants, thus hazardous to the environment. Dye-sensitized solar cells (DSSCs), which mimic photosynthesis in plants, are examples of third-generation photovoltaic (PV) technologies that are seen to be promising substitutes for solar energy harvesting. These cells are easier to fabricate, cheap, and have an outstanding indoor photon-to-current conversion efficiency [2, 3]. The structure of a typical DSSC comprises a working electrode (usually titanium dioxide (TiO_2) photosensitized using a dye (usually a Ruthenium complex)), an electrolyte (triodide/iodide), and a counter electrode (usually Pt) whose internal working processes are as explained in other literature [4–6]. Recent research advances on DSSCs have focused on improving electron transport and reducing the recombination rate using semiconductor materials other than TiO_2 [7–10]. Among the feasible alternatives is Zinc oxide (ZnO), an n-type semiconductor with a wide bandgap of about 3.37 eV and is nontoxic has been widely investigated [11, 12]. ZnO can be processed

chemically or biologically. Chemical synthesis involve the use of two or more precursor chemicals, which render the process toxic, expensive, and energy-intensive [5]. However, biological methods using plant extracts (green synthesis) as reducing and capping agents, attributed on their phytochemical compounds offer a more economical, sustainable, and environmentally friendly approach to producing metal oxide nanoparticles. In addition, green synthesis results in the production of well-dispersed and stabilized nanoparticles with varying morphologies fit for various applications [13] *Erythrina abyssinica* stem bark is rich in phytochemical compounds such as alkaloids, saponins, phenolics (flavonoids), tannins, and terpenoids, which are essential in the green synthesis of metal oxides [14]. In this article, we report the structural, electronic, and optical properties of ZnO by computational and experimental methods as a photoanode in DSSCs. We used the open-source code Quantum Espresso software to study the atomic insights of ZnO and then experimentally synthesized ZnO NPs using *Erythrina abyssinica* stem bark extract to reduce Zinc nitrate hexahydrate to ZnO NPs and applied them as a photo-anode for DSSC. Using a standard ruthenium dye (Ru-N719) as a photon absorber, the fabricated DSSC exhibitd a P_{MAX} of 2.39 μW cm^{-2}, J_{sc} of 56 μA cm^{-2}, V_{oc} of 161 mV, and a PCE of $2.39 \times 10\%^{-3\%}$ under one-sun illumination.

2. Materials and methods

2.1. Theoretical (First-Principles) approach

First principles calculations were performed using the self-consistent plane wave PWSCF code available in the Quantum Espresso open-source package based on the DFT for ground state calculations described by time-independent DFT KS equations [15]. The electronic exchange correlation energy was treated using the GGA parameterized by Perdew, Burke and Ernzerhof (PBE) [16]. The ultrasoft Pseudo potentials of PBEsol were employed for the electron–ion interaction.

The strongly correlated electronic nature of the 3d-electrons in Zn and 2p-electrons in O was corrected with the Coulomb correction in the framework of PBEsol + U with $U_{Zn\text{-}3d} = U_{O\text{-}2p} = 8.0$ eV [17, 18]. For the PW basis, we individually applied 40 Ry for cutoff energies and 500 Ry for charge density. The Brillouin zone was sampled with a $6 \times 6 \times 4$ Monkhorst–Pack K-point mesh for optimization of the structure, and the K-point mesh of $15 \times 15 \times 9$ was employed for the calculations of the DOS.

The optical properties were studied using the dielectric function $\varepsilon(w)$ in (1).

$$\varepsilon(w) = \varepsilon_1(w) + i\varepsilon_2(w) \tag{1}$$

where $\varepsilon_1(w)$ and $\varepsilon_2(w)$ are the real and imaginary parts of the dielectric function, were used to calculate the refractive index and absorption coefficient of ZnO.

2.2. Experimental section

2.2.1. Materials

Zinc nitrate hexahydrate, ethanol (99.99% purity), polyethylene glycol (PEG), iodide, hexachloroplatinic powder, Ruthenium dye (Ru N719). Fluorine-doped tin oxide (FTO) glass substrate, and distilled water. All chemicals were obtained from Sigma Aldrich and were used without further purification. *Erythrina abyssinica* stem bark was obtained from Ugandan flora, Matuba village, Mayuge district.

2.3. Plant extract preparation

Stem barks of the *Erythrina abyssinica* plant were cleaned using distilled water and dried, and ground into powder using a mortar and pestle. 10.0 g of the powder was dissolved in 100 ml of distilled water, placed on a hot plate and heated at 70 °C for 1 h. The cool mixture was then sieved using Whatman filter paper (Cat No 1001 125) to eliminate any residual solids. This was followed by centrifugation at 2400 rpm for 15 min to obtain the plant extract needed for green synthesis.

2.4. Synthesis of ZnO nanoparticles

5.0 of zinc nitrate Hexahydrate was added to 15 mL of the plant extract and heated at 70 °C under magnetic stirring for 2 h. The resultant precipitate was placed in an oven at 120 °C for 12 h. The particles were then calcined in a furnace at temperatures of 300, 400, 500, and 700°C for 2 h.

2.5. Preparation of the electrodes

2.5.1. Fabrication of the counter electrode

The FTO glass substrates were cleaned with distilled water, followed by ethanol for 30 min in an ultrasonic bath. 2.0 mg of hexa-chloroplatinic powder was dissolved in 1 mL of ethanol and stirred uniformly for 15 min. The FTO substrates were side-covered with a one layer of scotch tape, which had a thickness of 0.06 mm. The

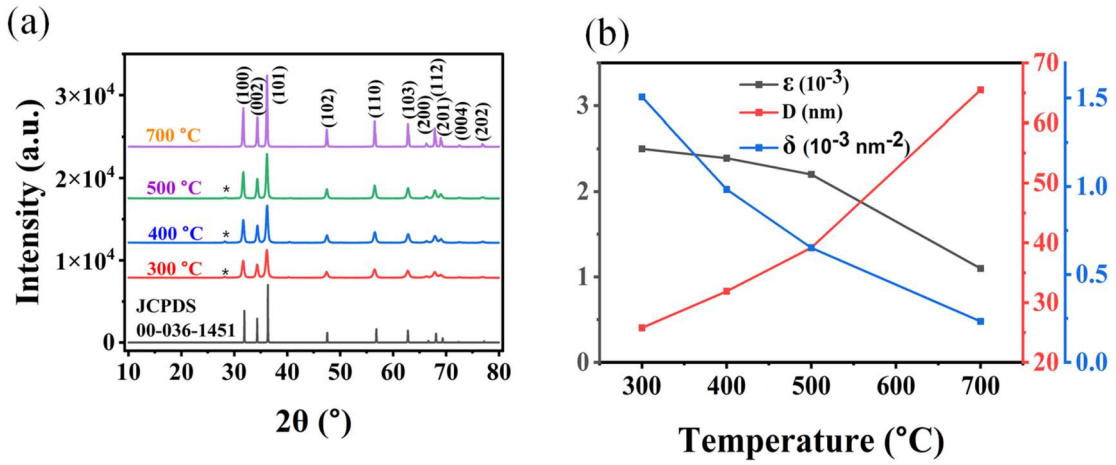

Figure 1. (a) XRD pattern of bio-synthesized ZnO NPs and (b) variation of average particle size (D), micro-strain (ε), and dislocation density (δ) with temperature.

solution was drop-cast on a pre-cleaned FTO substrate using a 200 μm pipette. The samples were kept for 24 h to evaporate the solvent at room temperature before being annealed at 400 °C for 15 min.

2.5.2. Fabrication of photoanode

1.0 g of ZnO NPs was added to a mixture of 0.4 g of PEG in 5 mL of glacial acetic acid and 5 mL of distilled water. The resultant mixture was sonicated for 2 h and then drop-cast on a pre-cleaned FTO substrate and left to dry. The dry film was annealed in a furnace at 300 °C for 1 h before photosensitizing it by immersing it in the dye extract for 24 h. The sensitized film was rinsed with ethanol and applied as a photo-anode. The thickness of the ZnO film was estimated to be 0.06 mm.

2.6. Preparation of liquid electrolyte

0.127 g of iodine and 0.83 g of potassium iodide were dissolved in 10 mL of ethylene glycol and uniformly stirred until completely dissolved. The solution was then kept in an amber bottle for further use.

2.7. Characterization methods

The crystal structural properties of ZnO NPs were studied using a SHIMADZU XRD-700 x-ray diffractometer (XRD) (Cu-K_α radiation, $\lambda = 1.5406$ Å). The functional groups in the ZnO NPs were identified using a Fourier Transform Infrared (FTIR) spectrophotometer SHIMADZU (IRTracer-100). A Gemini 1 ZEISS scanning electron microscope (SEM) was used to examine the surface morphology of ZnO NPs, and the elemental composition of the ZnO nanoparticles was investigated using energy-dispersive x-ray spectroscopy (EDX). UV–visible–NIR spectrophotometer was used to investigate the optical properties of ZnO NPs in the 200–1100 nm range. The photoluminescence (PL) properties of the ZnO nanoparticles were investigated using an FL spectrometer instrument with a 350-nm laser source [19, 20].

2.8. Assembly of DSSC and current–voltage (*I-V*) measurements

The ZnO photo-anode and Pt counter electrode were sandwiched firmly using clips, and an electrolyte was injected between the electrodes using a syringe. The solar cell performance was tested using a solar simulator under standard conditions on an active area of 0.25 cm^2 (AM 1.5 100 mW cm^{-2}), and the *J-V* characteristics were recorded using Keithley SMU-2450.

3. Results and discussion

3.1. Crystal structural properties

Figure 1(a) shows the XRD pattern of ZnO NPs, which was in good agreement with the standard pattern of space group $P6_3mc$ (JCPDS number 00–036–1451), confirming the hexagonal phase (Wurtzite structure) of ZnO NPs. The diffraction peaks at $2\theta = 31.67, 34.35, 36.16, 47.47, 56.52, 62.82, 66.31, 67.90, 69.03, 72.54$, and 76.92° corresponded to diffraction planes of (100), (002), (101), (102), (110), (103), (200), (112), (210), (004), and (202) respectively as shown in figure 1. The extra peak at 28.30° marked as (*) at temperatures of 300, 400, and 500 °C was due to the impurity phase of Zn $(OH)_2$ in ZnO. It was observed that this impurity peak

Table 1. Calculated average crystallite size, micro-strain, dislocation density, band gaps, and lattice constants of ZnO NPs.

					Lattice constants		
T (°C)	D (nm)	ε	δ (nm^{-2})	E_g (eV)	a (Å)	c (Å)	V (Å^3)
300	25.8	0.0025	0.00151	3.20 ± 0.04	3.2627	5.2124	55.49
400	31.9	0.0024	0.00098	3.19 ± 0.04	3.2597	5.2128	55.39
500	39.2	0.0022	0.00065	3.16 ± 0.04	3.2577	5.2135	55.33
700	65.5	0.0011	0.00023	3.12 ± 0.03	3.2568	5.2138	55.30

diminished as the calcination temperature was increased until it disappeared at 700 °C. In the XRD analysis, it was noted that the full width at half maximum (FWHM) decreased with an increase in the calcination temperature, which led to narrower and sharper peaks with increased intensities at higher temperatures. Thus, highly crystalline and pure ZnO NPs were obtained at 700 °C, and a similar trend was reported in other studies [21, 22].

The impact of crystallite size (D) and lattice strain on the widening of diffraction peaks can be represented by the Williamson–Hall (W–H) equation (2).

$$\beta_{hkl} \cos\theta = \frac{K\lambda}{D} + 4\varepsilon \sin\theta \tag{2}$$

where D is the crystallite size, K is the shape factor (0.9), $\lambda = 1.5406$ Å, θ is the diffraction angle, and β_{hkl} is the full width at half maximum (FWHM) corresponding to the (hkl) diffraction plane, and ε is the micro-strain. Crystallite size and micro-strain can be derived from the intercept ($\frac{K\lambda}{D}$) and slope ε in the W–H plot of $\beta_{hkl} \cos\theta$ against 4 sin θ, respectively. The dislocation densities, δ, of the samples were calculated using equation (3), and all the resulting values were recorded as shown in table 1.

$$\delta = \frac{1}{D^2} \tag{3}$$

Table 1 shows that the crystallite size increased from 25.8 to 65.5 nm with an increase in the calcination temperatures. This is attributed to the growth of particles as a result of an interfacial reaction [23]. The dislocation densities and micro-strain both decreased with a rise in the calcination temperature, as shown in figure 1(b). This means that the lattice defects gradually diminished, leading to improvement in the crystallinity of the ZnO NPs at the higher temperature [23]. The calculated lattice constants for the bio-synthesized ZnO NPs ranged from $a = b = 3.2627$ Å at 300 °C to 3.2568 Å at 700 °C and $c = 5.2124$ Å at 300 °C to 5.2138 Å at 700 °C as indicated in table 1. An increase in calcination temperature led to a significant decrease in lattice parameter a with a slight increase in lattice parameter c, which in turn led to a decrease in the unit cell volume. The increase in temperature resulted in a more structured arrangement of crystals within the lattice, featuring fewer impurities and enhanced density, which reduced the lattice parameters and consequently diminished the volume of the unit cell [24].

3.2. Functional groups analysis

The FTIR spectra revealed potential functional groups of the synthesized ZnO NPs. These showed the presence of Zn-O bonds in the fingerprint region in all samples, as shown in figure 2. The presence of the Zn-O matched well with the XRD spectra indicating that ZnO NPs were successfully processed. Also in the finger print region, the FTIR spectra revealed a possibility of a Sp^3 C-O functional group in the samples. In the functional group region, the C=C (aromatic rings), C≡C, C = O (carbonyl), and Sp^3 C-H stretches were also identified [25, 26]. All samples indicated the presence of the O-H (hydroxyl) group, which is crucial for the chemical attachment of the photosensitizing dye onto the ZnO thin film for use as a working electrode in DSSCs. The corresponding frequency wavenumbers at which the various functional groups are cited in the different ZnO NPs calcined at 300 °C from figure 2 (a), at 400 °C from figure 2 (b), at 500 °C from figure 2(c), and at 700 °C from figure 2 (d) have been summarized in table 2.

3.3. Surface morphology of ZnO nanoparticles

Figures 3(a)–(d) show the SEM images of ZnO NPs at calcination temperatures of 300, 400, 500, and 700 °C.

The images indicate variations in levels of agglomeration depending on the growth temperature. The micro-images in figures 3 (a)–(c) show incomplete nucleation and growth process, non-uniform, flake-like, agglomerated particles surrounding spherically shaped nanoparticles. This agglomeration is due to the polarity

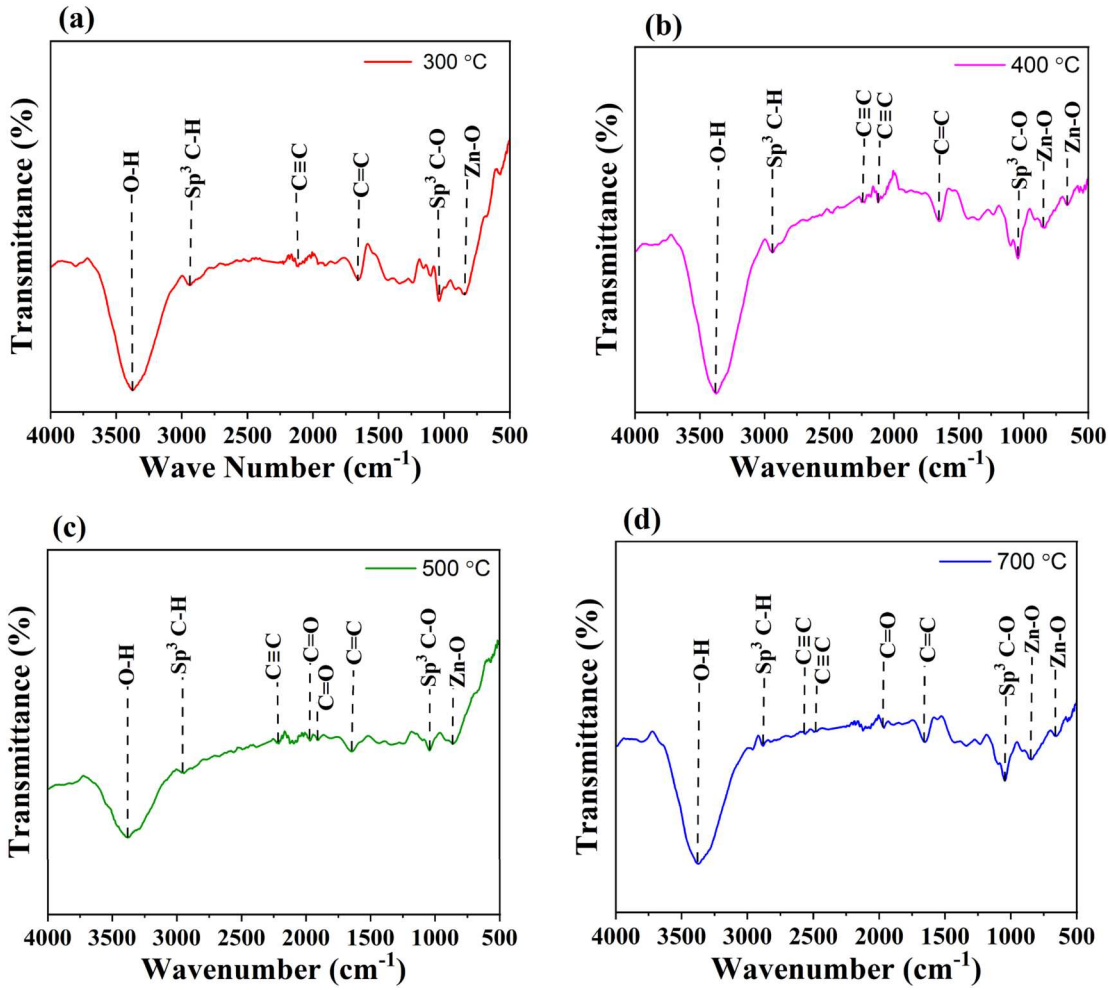

Figure 2. FTIR spectra for ZnO NPs calcined to different temperatures of (a) 300 °C, (b) 400 °C, (c) 500 °C, and (d) 700 °C.

and electrostatic, high surface energy, van der Waals forces, or other interparticle interactions. The presence of spherical nanoparticles alongside the flake-like particles suggests a possible bimodal distribution of particle sizes and shapes. Spherical particles often form due to minimization of surface energy [27]. However, at a calcination temperature of 700 °C, the particles become more distinguishable. This is due to the formation of larger particles at higher calcination temperatures, primarily due to grain growth and particle agglomeration. As the temperature rises, the crystallites that form get bigger and nearby particles are more likely to fuse, creating a more compact and ordered structure as opposed to separate nanoparticles [28–30]. This is in good agreement with the XRD findings, which showed that particle size increased with an increase in calcination temperature. Hence, the micro-images illustrate that temperature has a direct impact on the surface morphology of a material.

The elemental composition of ZnO NPs was determined through Energy Dispersive X-ray spectroscopy (EDX). The insets in figures 3(a)—(d) display the peaks and corresponding elements for each sample in the prepared ZnO NPs. EDX identified Zn, O, and C at 300 °C and 400 °C, while only Zn and O were detected at 700 °C, with wt% of 72.93% and 27.07%, respectively, indicating the formation of pure ZnO [22]. The presence of carbon (C) likely originated from biomolecules in *Erythrina abyssinica* stem bark at 400 °C and below, which volatilized at higher calcination temperatures.

3.4. Optical properties of ZnO NPs

Figure 3(a) shows the PL spectra of bio-synthesized ZnO nanoparticles using *Erythrina abyssinica* stem bark extract. The PL spectra of ZnO NPs at room temperature (RT) show two main emission peaks corresponding to deep level defects (DLE) and band-to-band emissions (BBE) in the visible and ultraviolet (UV) regions, respectively [29]. One peak near the UV region, attributed to BBE through excitation collision processes, and a broad peak in the visible region due to deep-level emissions caused by oxygen, around 560 nm (green region) [30, 31]. However, it was observed that increasing the calcination temperature significantly enhanced the

Table 2. Vibration frequency numbers for the respective functional groups present in the calcined ZnO NPs.

Calcination Temperature (°C)	Frequency Number (cm^{-1})	Functional Groups
300	844.73	Zn-O
	1036.25	Sp^3 C-O
	1649.91	C = C
	2115.14	C≡C
	2939.47	Sp^3 C-H stretches
	3384.75	O-H
400	658.00 and 839.95	Zn-O
	1036.25	Sp^3 C-O
	1649.91	C = C
	2124.72 and 2234.84	C≡C
	2939.47	Sp^3 C-H stretches
	3370.38	O-H
500	849.52	Zn-O
	1041.04	Sp^3 C-O
	1635.54	C = C
	1908.46 and 1971.50	C = O
	2210.90	C≡C
	2949.04	Sp^3 C-H stretches
	3375.17	O-H
700	653.21 and 839.95	Zn-O
	1041.04	Sp^3 C-O
	1645.12	C = C
	1961.92	C = O
	2483.81 and 2560.42	C≡C
	2882.01	Sp^3 C-H stretches
	3370.38	O-H

intensity of peaks in the blue region (420–480 nm), while the peak intensity in the UV spectrum markedly decreased. This change results from an increase in Zn vacancy defects facilitated by higher temperature, leading to prominent deep-level emissions and reduced band-to-band emissions [30]. We further investigated the optical properties of the bio-synthesized zinc oxide nanoparticles using diffuse reflectance spectra (DRS), as shown in figure 3(b). In reflection spectra, lower reflectance indicates higher absorption at the corresponding wavelength, and vice versa. The reflectance spectra for all samples are quite similar in the UV wavelength range of 310–377 nm. However, notable differences appear between the RT sample and those calcined at 300, 400, 500, and 700 °C in the visible range of 400–760 nm. The reflectance (R) was then converted to an equivalent absorption spectrum using the Kubelka–Munk (KM) function, explained in detail elsewhere [26, 27, 32]. The KM function is given by equation (4).

$$F(R) = \frac{(1 - R)^2}{2R} \tag{4}$$

A Tauc plot of $(\alpha h\upsilon)^2$ versus $h\upsilon$, as shown in (5), was generated. Using a linear fit, the band gaps were estimated and are summarized in table 1.

$$(\alpha h\upsilon)^r = A(h\nu - E_g) \tag{5}$$

where E_g is the energy band gap, $\alpha = F(R)$ is the absorption coefficient, $h\upsilon$ is the photon energy, A is a constant that depends on the material, and r is 2 if the transition is a direct one or 0.5 if the transition is indirect. All the samples show absorption bands in the λ_{max} region below 600 nm, as seen in figure 4(c). The absorption maximum of the samples calcined at 300, 400, 500, and 700 °C indicates a shift towards the blue line of the spectrum. The results also show that the bandgap of the semiconductors is temperature-dependent. The optical bandgap energies for ZnO nanoparticles were calculated to be 3.20 and 3.19 eV at temperatures of 300 and 400°C, respectively, while at temperatures of 500 and 700 °C, the optical bandgap energies were 3.16 and 3.12 eV, respectively. These results fall in the reported bandgap range of 3.10–3.39 eV for ZnO nanoparticles [31, 33]. The increase in calcination temperature resulted in grain growth with decreased defects, thus improving the crystallinity of the synthesized ZnO NPs, as supported by the SEM and XRD analysis. The ZnO NPs become less amorphous with a rise in the calcination temperature, giving a decreased band gap [5].

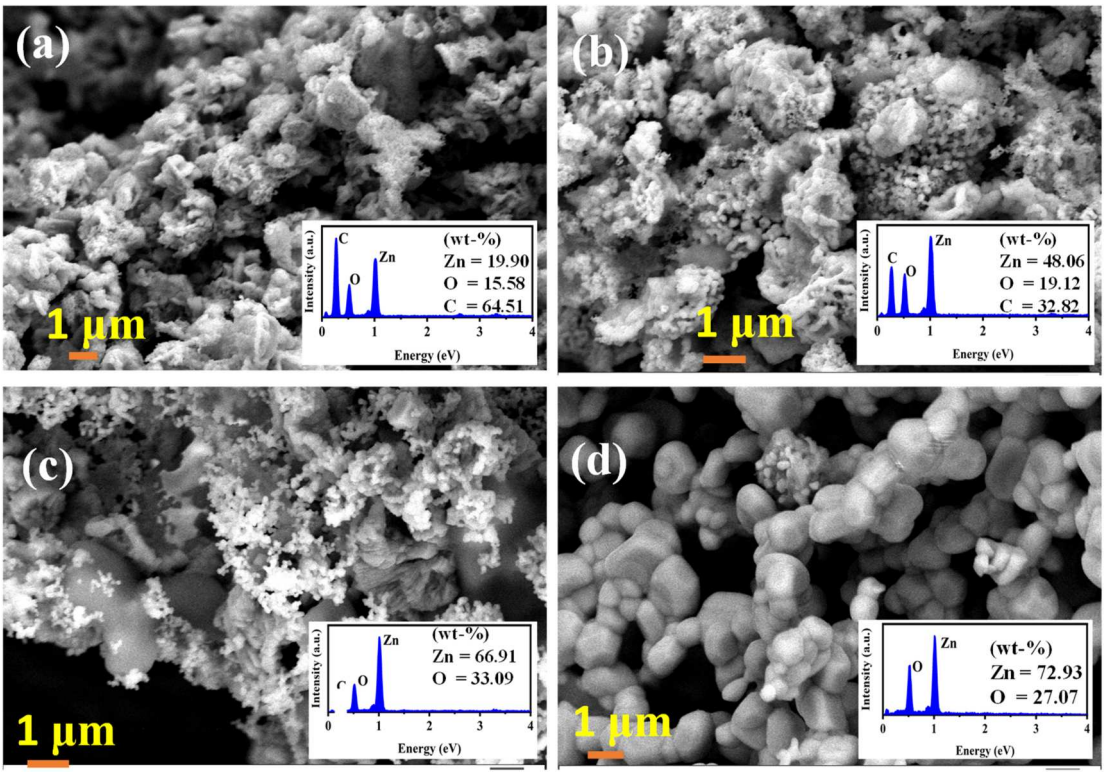

Figure 3. SEM images for ZnO nanoparticles calcined at (a) 300, (b) 400, (c) 500, and (d) 700 °C with their respective EDX spectra (insets).

3.5. Device *J-V* analysis

Figures 5(a) and (b) show the current density–voltage (*J-V*) and power density–voltage (*P-V*) characteristics of the as-fabricated solar cell using ZnO as the photo electrode. The power conversion efficiency (PCE, η) and fill factor (FF) were evaluated using (6) and (7).

$$\eta = \frac{P_{\max}}{P_{in}} \times 100\% \tag{6}$$

$$FF = \frac{J_{\max} V_{\max}}{J_{sc} V_{oc}} \tag{7}$$

where $J_{\max}$ and $V_{\max}$ are the current density and voltage, respectively, at maximum power output, J_{sc} is the short circuit current, V_{oc} is the open circuit voltage, $P_{\max}$ is the maximum power generated by the solar cell, and P_{in} is the incident power density of the solar simulator (100 mW cm^{-2}). The cell device demonstrated an η of ~ 0.0024% with a J_{SC} of 56 µAcm^{-2}, V_{OC} of 161 mV, and FF of 0.265 under one-sun illumination. The device's poor PCE could be due to Zn^{2+}/dye clusters increasing the recombination reactions between the photo-injected electrons and the redox(I_{3-}) components [34]. This greatly limits the number of these photo-generated electrons conducted across the external circuit, and thus very low short circuit density. However, its fill factor of 0.265 was remarkably higher than 0.118, reported by Abdullah *et al* [35]. These underperformances of ZnO-based photoanodes are reported in different literature as shown in table 3. This showed that the performance of a cell based on ZnO photoanode also depends on synthesis techniques that produce NPs with unique properties. The device's stability was evaluated after 28 days, showing a reduction in power conversion efficiency of 0.00048%, with a J_{sc} of 8.8 µAcm^2, V_{oc} of 240 mV, and P_{max} of 0.48 µW/cm^2. The decrease in PCE suggests instability of the device over the 28 days, and is a major challenge in DSSC devices. However, further studies would be needed to assess long-term stability and potential degradation mechanisms.

3.6. DFT structural calculations

Figure 6(a) shows the visualized lattice structure of ZnO, which contains four atoms in its unit cell. The lattice parameters a, c/a ratio, and c are summarized in table 4, calculated from PBEsol, PBEsol+U, and experimental data. Figures 6(b) and (c) illustrate the convergence of the lattice parameters of ZnO in PBEsol and PBEsol+U calculations, and the findings are compared to experimental and theoretical data previously reported in the literature [40].

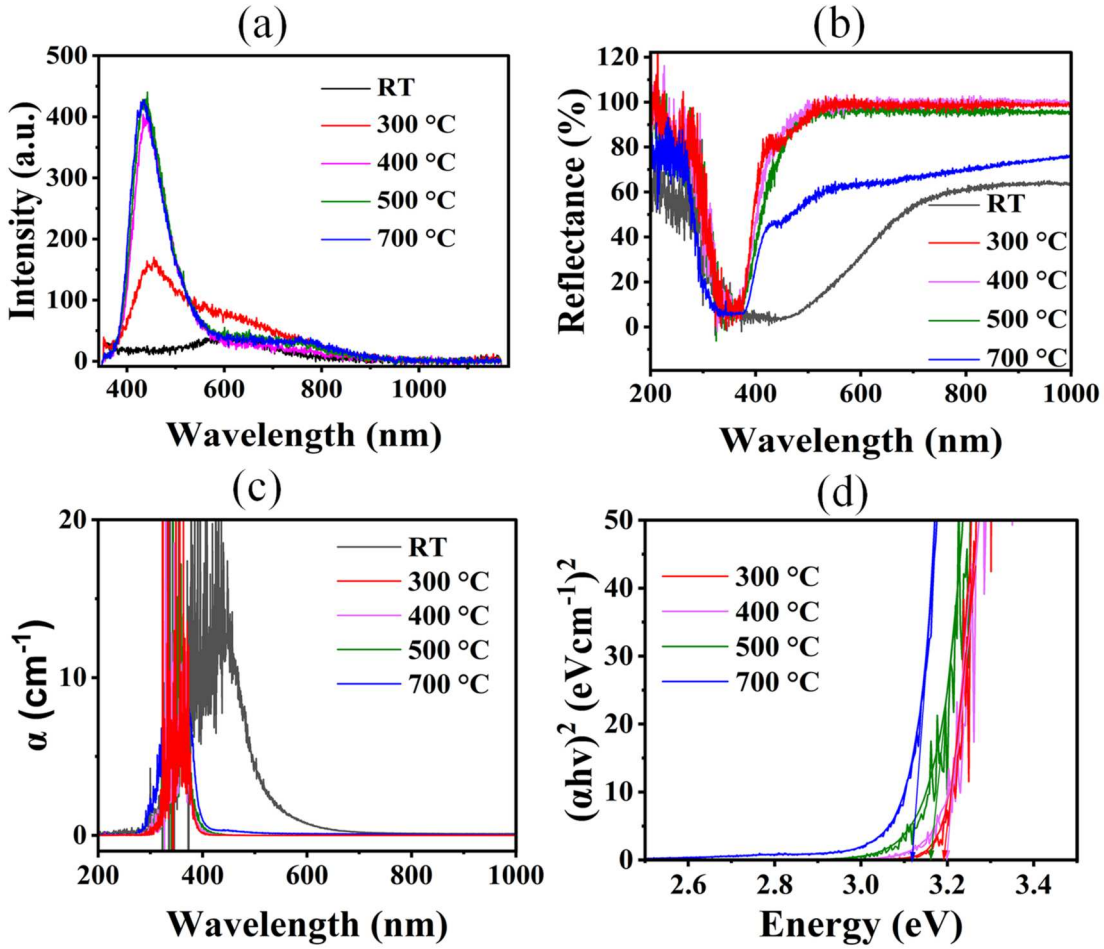

Figure 4. (a) Photoluminescence spectra of ZnO NPs, (b) DRS spectra of ZnO NPs synthesized at room temperature (RT), 300, 400, 500, and 700 °C, (c) UV–Visible absorption spectrum of ZnO NPs, and (d) Tauc plots for the bio-synthesized ZnO NPs.

The optimized lattice parameters of ZnO using PBEsol are $a = 3.2562$ Å and $c = 5.2591$ Å, which were in good agreement with the experimental values obtained in this work ($a = 3.2568$ Å, $c = 5.2134$ Å), as indicated in table 4. However, PBEsol slightly overestimated c with an error of 0.876% compared to the experimental value. These variations are in line with the overall pattern observed in DFT techniques based on PBEsol, which occasionally overestimate bond lengths by a small amount due to underbinding effects [40]. When the Hubbard U correction was included to PBEsol, *a* and *c* changed to 3.2186 and 5.2151 Å, respectively. This shows a contraction in a unit cell and *a* larger *c*/*a* ratio (1.6203), which differs from the experimental *c*/*a* of 1.6008. The increasing localization of Zn-3d and O-2p electron states brought on by the U parameter is responsible for this change. The lattice parameters are consistently over-/under estimated by traditional PBE-based DFT+U, leading to slight errors in structural predictions, though they are well known for correcting the electronic structure [40]. Overall, the PBEsol technique showed greater accuracy in replicating the experimental ZnO lattice parameters. This demonstrates how structural predictions are sensitive to the physical origin of the experimental sample as well as computational inputs such as convergence thresholds, exchange–correlation functionals, or pseudo-potentials [41].

3.7. Electronic calculations

Figure 7 shows the calculated band structures and PDOS of ZnO (wurtzite) using standard PBEsol and PBEsol +U with the Fermi level set to zero. Figures 6 (a) and (b) show that ZnO exhibits a direct band gap at Gamma (Γ), which is in good agreement with the experimental findings in figure 4(d). Thus, the electron transition from the valence band (HOMO) to the conduction band (LUMO) in ZnO occurs at Γ. The calculations from PBEsol estimated a band gap of 0.75 eV, which is significantly lower than the experimental band gaps of 3.12–3.20 eV reported in this work. The underestimation of band gaps of ZnO in DFT was reported in previous work by Duong (2024) [42]. This is attributed to DFT's limitation in capturing self-interaction effects in electrons, leading to overestimation in the binding energy of electrons in the occupied states. These self-interaction errors lower the energy of the occupied states relative to unoccupied states, thereby producing a

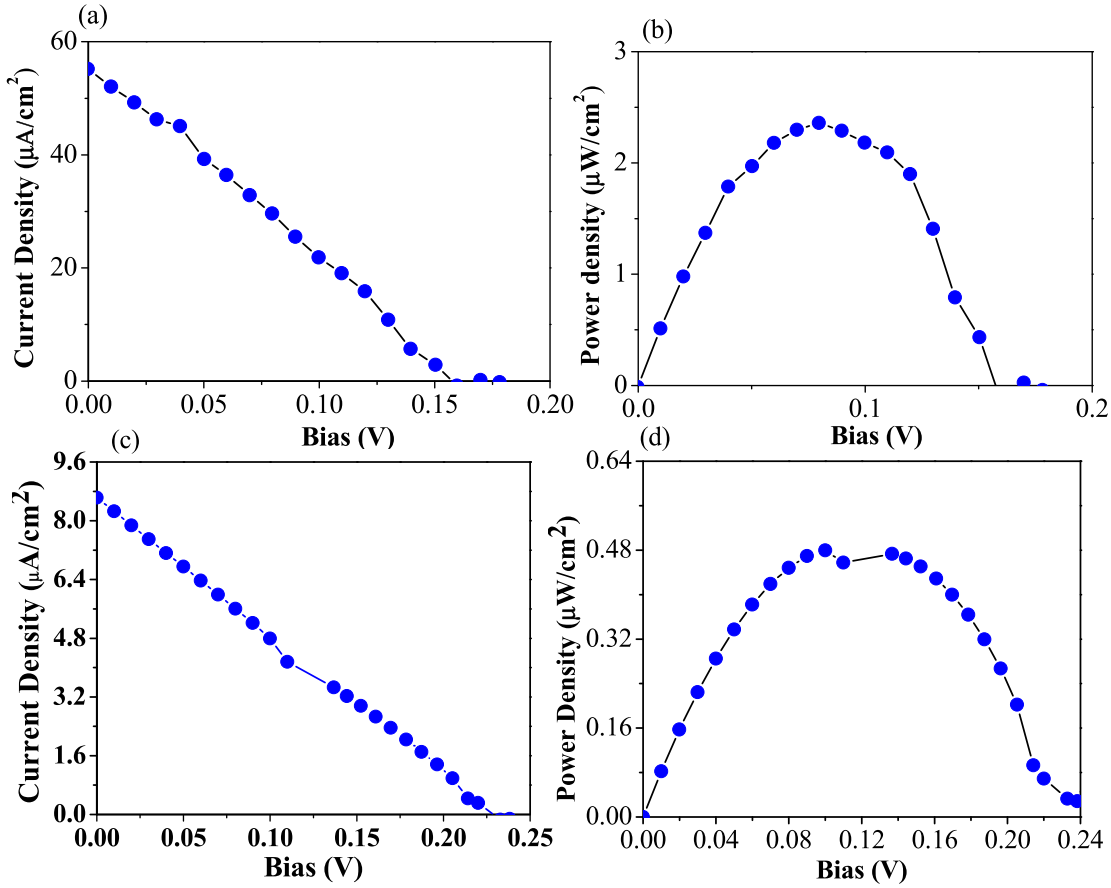

Figure 5. (a) & (b) *J-V* and *P-V* characteristic curves of the as-fabricated solar cell device, (c) & (d) *J-V* and *P-V* characteristic curves of the fabricated solar cell device after 28 days.

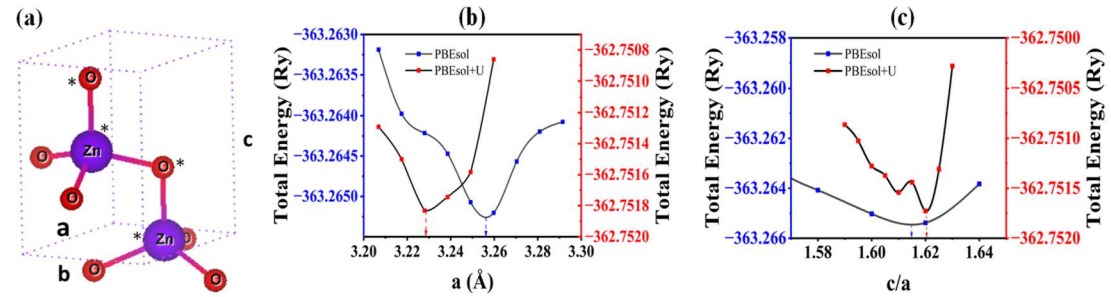

Figure 6. (a) unit cell of ZnO with four atoms marked (*) and Lattice parameter convergence of ZnO using (a) PBEsol and (b) PBEsol +U.

Table 3. Comparison of efficiency values for a few selected DSSCs based on ZnO nanoparticle photoanode.

Photoanode Electrode	Synthesis method	PCE (%)	References
ZnO	Hydrothermal	6.7×10^{-1}	[36]
ZnO	Hydrothermal	2.9×10^{-1}	[37]
ZnO	Solvothermal	2.0×10^{-2}	[38]
ZnO	Chemical bath deposition	3.0×10^{-3}	[35]
ZnO-2 nm thickness	Screen-printing	8.0×10^{-2}	[39]
ZnO	Green synthesis	2.4×10^{-3}	This study

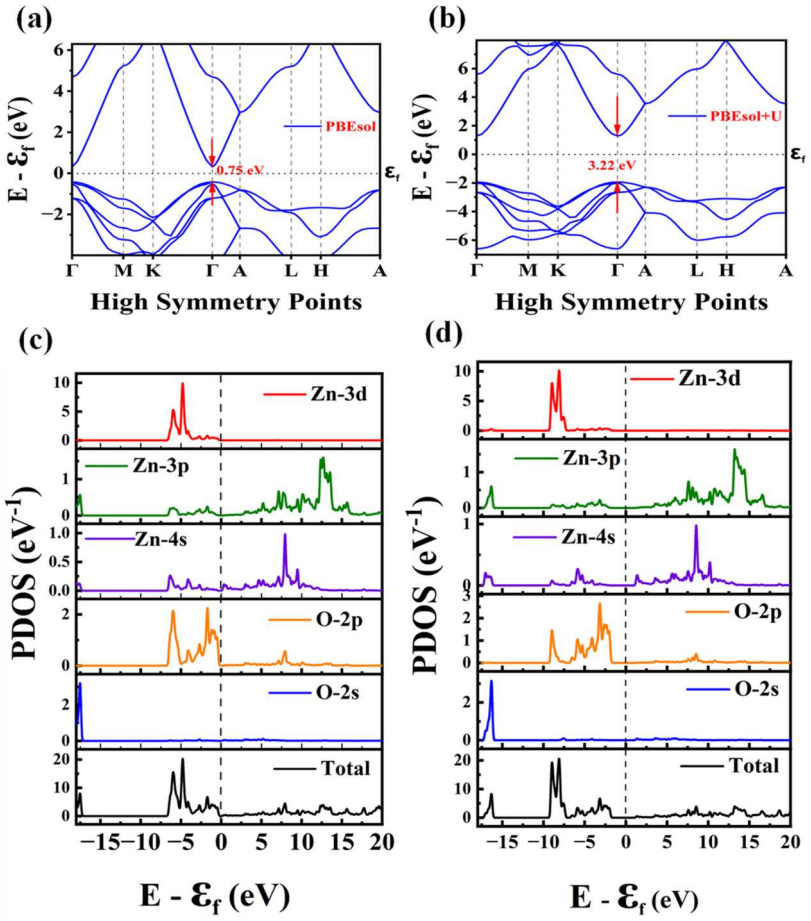

Figure 7. (a) and (b) show the electronic band structures of ZnO, showing the valence and conduction bands using PBEsol and PBEsol+U, respectively, and (c) and (d) show their respective projected density of states.

Table 4. Lattice parameters of ZnO (wurtzite) predicted by the PBEsol and PBEsol+U and experimental analysis compared to those reported in the literature.

Approach	a (Å)	c/a	c (Å)	References
PBEsol	3.2562	1.6151	5.2591	This work
PBEsol+U	3.2186	1.6203	5.2151	This work
Exp.	3.2568	1.6008	5.2134	This work
DFT	3.3169	1.6087	5.3359	[40]
DFT+U	3.2764	1.6043	5.2563	[40]
Exp.	3.2577	1.6007	5.2146	[40]

narrower band gap. The PBEsol+U with $U_{3d} = U_{2p} = 8.0$ eV pushed away the VBM and CBM from the Fermi level, thus widening the band gap to 3.22 eV, matching the experimental prediction as shown in figure 7(b).

Thus, the addition of the Hubbard parameter effectively decreased the energy of 3d states of Zn, lowering their hybridization with the 2p states of O within the VB because of reduced repulsions. Consequently, a more precise and accurate description of the energy gap between the valence band and conduction band is obtained. Figure 7(c) shows that the 2p-states of O dominate the valence band in the region from −4.5 eV up to the VBM, and the Zn-3d states are situated deep within the valence band in the energy range from −6.5 eV to −4.0 eV. This indicates some degree of formation of Zn-O covalent bond due to the noted weak hybridization of the localized Zn-3d states with the O−2p orbitals. In figure 7(d) for PBEsol+U, the Zn-3d states are pushed further to lower energy regions, separating them significantly from the O−2p states. Hence, an improved physical interpretation of the electronic structure of the highly localized d-electrons in ZnO is due to reduced hybridization with the 2p orbitals of O. The O-2p states become more concentrated and distinct around the valence band maximum. This correction reduces the self-interaction error observed in the standard DFT (PBEsol), which

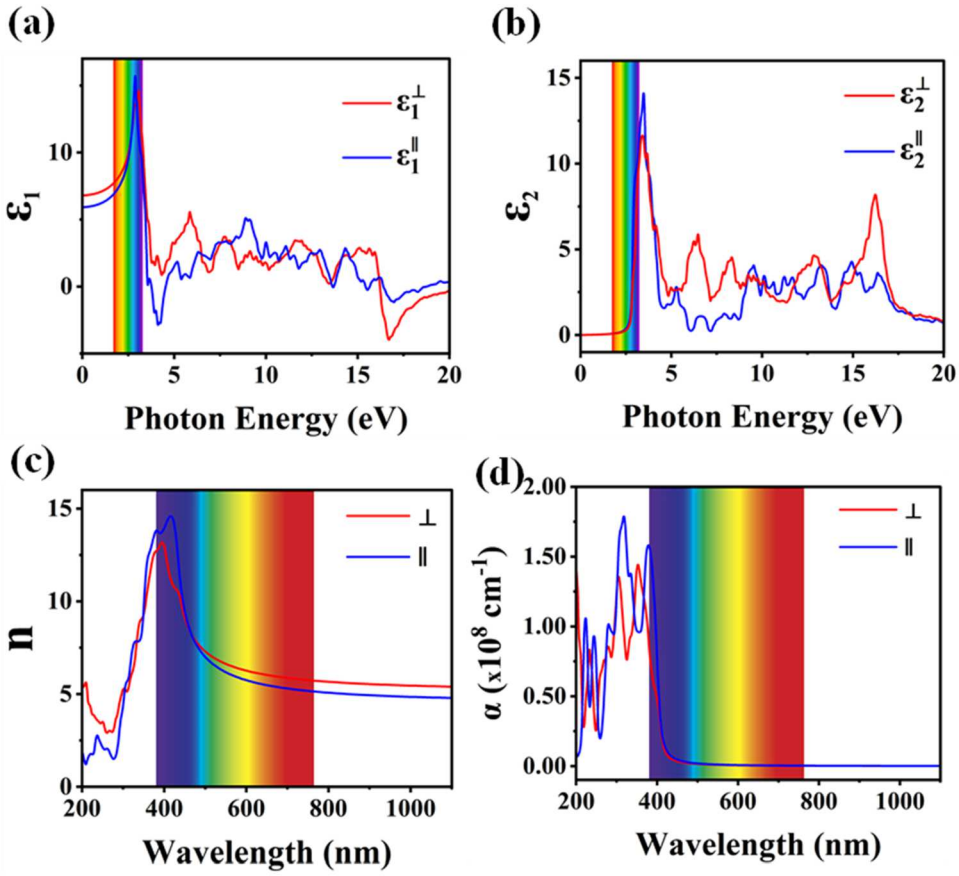

Figure 8. (a) dielectric real part, (b) dielectric imaginary part, (c) refractive index, and (d) absorption coefficient of ZnO.

wrongly places the Zn-3d states very near to the VBM. Both PBEsol and PBEsol+U reveal a significant contribution from Zn−4s and Zn-3p states in the conduction band, with almost unnoticeable O-derived states.

3.8. Calculations on dielectric function

Through the real (ε_1) and imaginary (ε_2) components of the dielectric function, the refractive index $n(w)$, and absorption coefficient $\alpha(w)$ as functions of photon energy and wavelength, the optical properties of ZnO were examined using equations (7) and (8), differentiating between polarization directions parallel ($\|$) and perpendicular ($\perp$) to the crystallographic *c*-axis [43]. Understanding the material's interaction with electromagnetic radiation in the visible, near-infrared (NIR), and ultraviolet (UV) spectral areas was achieved by evaluating these properties.

$$n(w) = \sqrt{\frac{\sqrt{\varepsilon_1^2(w) + \varepsilon_2^2(w)} + \varepsilon_1(w)}{2}} \tag{7a}$$

$$\alpha(w) = \frac{w}{c}\sqrt{\frac{\sqrt{\varepsilon_1^2(w) + \varepsilon_2^2(w)} - \varepsilon_1(w)}{2}} \tag{8}$$

where w and c are the frequencies and speed of light in a vacuum.

The real and imaginary parts of the dielectric function as a function of photon energy (0–20 eV) are shown in figures 7(a) and (b). The dispersive response of the material is characterized by the real portion, $\varepsilon_1(\omega)$. At low photon energies, ε_1 for ZnO exhibits high values, peaking just below 3 and reaching a maximum for both $\varepsilon_1^{\perp}$ and $\varepsilon_1^{\|}$ polarizations, revealing its static dielectric constant. The material's absorptive response is represented by the imaginary component, $\varepsilon_2(\omega)$, which shows a notable anisotropy between the polarization orientations. According to our calculations of the $\varepsilon_2(\omega)$ spectra, the dielectric function's threshold energy, or first critical point, is located at about 3.20 eV. This is in line with the Γ_v–Γ_c separation, which provides the threshold for direct optical transitions between the CBM and the VBM. For light polarized perpendicular to the *c*-axis, the $\perp$ polarization regularly exhibits larger ε_2 values than the $\|$ direction, indicating stronger optical transitions. In the optical response, the electric-dipole transitions between the valence and conduction bands are what explain

the presence of extra peaks beyond 3.20 eV is evidence of different interband transitions involving deeper conduction and valence states in ZnO [44].

In figures 8(c), (a) peak is observed in the UV region (~350–400 nm) of the refractive index spectra. But the refractive index steadily decreases and remains constant through the visible and infrared regions. Interestingly, the || polarization has a little lower refractive index throughout the spectrum than the ⊥ direction. In figure 8(d), the absorption coefficient $\alpha(w)$ indicates a high absorption onset close to 375–400 nm, which is in line with ZnO's optical bandgap. α can reach values of more than 1.5×10^8 cm^{-1} in the UV range (<400 nm), where the || polarization shows stronger absorption than the ⊥ direction. This suggests low reflectivity, little absorption, and good transparency of ZnO in the visible to near-infrared (>400 nm) regions; however, the high refractive index and strong absorption in the UV range imply strong light–matter interaction, which is advantageous for UV photonic applications.

4. Conclusion and way forward

In this study, we performed DFT calculations and synthesized highly crystalline ZnO NPs with a crystallite size of 65.5 nm using aqueous stem back extract of the *Erythrina abyssinica* plant at 700 °C. SEM images revealed non-uniform, flake-like, highly agglomerated structures around the spherical nanoparticles with a band gap of 3.12 eV at 700 °C. The PL spectra exhibited a major peak only in the blue region of the visible spectrum. The DSSC exhibited an efficiency of ~ 0.0024% with a V_{OC} of 161 mV, and J_{SC} of 56 μA cm^{-2} under 1 Sun illumination. The poor performance can be attributed to the limited light absorption in the visible spectrum by the Ru N719 dye adsorbed on biosynthesized ZnO nanoparticles, and fast electron–hole recombination rates. In addition, DFT calculations provided complementary insights with significant contributions of the Zn-4s and O-2p orbitals to the CBM and VBM in DOS, respectively, and a direct band gap at Gamma, in the electronic band structure, matching the experimental range. Calculations on the dielectric function revealed anisotropy in the refractive index and dielectric function, with noticeable transparency in the visible spectrum and strong absorption in the ultraviolet. Green-synthesized ZnO's effectiveness for solar applications is supported by the high correlation between experimental findings and DFT predictions. The study successfully synthesized ZnO NPs via green synthesis and showed their applicability in DSSCs, thus adding to other areas of application of green-synthesized ZnO NPs such as the biomedical science field, organic electronics, and in environmental applications. Although the study's performance results for DSSC photoanode application are low compared to other values obtained from conventionally synthesized ZnO photoanodes, the study has provided further experimental and theoretical insights on green synthesized ZnO nanoparticles for optoelectronic device applications. Future research should be focused on improving the light absorption range of Ru N719 dye adsorbed on biosynthesized ZnO nanoparticles and minimizing the charge recombination rates through doping and heterostructuring.

Acknowledgments

This work was carried out with the aid of a grant from UNESCO-TWAS financed by the German Federal Ministry of Education and Research (BMBF) (**No. 24-167 RG/PHYS/AF/AC_I—FR3240339180**). The views expressed herein do not necessarily represent those of UNESCO-TWAS, BMBF, or its Board of Governors. We further acknowledge the Kyambogo University Competitive Research Grant (9th Call) for the financial support.

Conflict of interest

The authors declare that there is no conflict of interest regarding the publication of this article.

Data availability statement

All data that support the findings of this study are included within the article (and any supplementary files).

Data and code availability

Not applicable.

Supplementary information

Not applicable.

Ethical approval

Not applicable.

Author contributions

Stephen Balabye
Conceptualization (equal), Data curation (lead), Formal analysis (lead), Methodology (lead)

Emmanuel Mushebo
Data curation (equal), Formal analysis (equal), Investigation (equal), Methodology (equal)

Stella Nasejje
Formal analysis (equal), Data curation (equal)

Egor Moses 0009-0006-9039-8113
Formal analysis (equal), Data curation (equal), Supervision (equal)

Emma Panzi Mukhokosi 0000-0001-9229-3821
Conceptualization (lead), Data curation (lead), Formal analysis (lead), Resources (lead), Supervision (lead)

References

[1] Kam C Z and Kueh A B H 2015 Towards sustainable polymeric materials: zero waste, green and self-healing *J Teknol* **74** 159–63
[2] Devadiga D, Selvakumar M, Shetty P and Santosh M S 2021 Dye-sensitized solar cell for indoor applications: a mini-review *J. Electron. Mater.* **50** 3187–206
[3] Das M and Chatterjee S 2019 Green synthesis of metal/metal oxide nanoparticles toward biomedical applications: Boon or bane *Green Synthesis, Characterization and Applications of Nanoparticles Micro and Nano Technologies.* (Elsevier Inc) 265–301
[4] Calogero G, Bartolotta A, Marco G D, Carlo A D and Bonaccorso F 2015 Vegetable-based dye-sensitized solar cells chemical society reviews vegetable-based dye-sensitized solar cells *Chem Sovciety Rev* **44** 3244–94
[5] Mukhokosi E P, Mushebo E, Nassejje S, Botha N L, Velauthapillai D and Maaza M 2025 Green synthesis of hematite nano flakes and their application as a counter electrode in dye-sensitized solar cells *Sci. Rep.* **15** 19837
[6] Chandra M, Chen L, Lai C, Lee Y, Chang C and Chen C 2020 Enhancement of power conversion efficiency of dye-sensitized solar cells for indoor applications by using a highly responsive organic dye and tailoring the thickness of photoactive layer *J. Power Sources* **479** 229095
[7] Palomares E, Clifford J N, Haque S A, Lutz T and Durrant J 2003 Control of charge recombination dynamics in dye sensitized solar cells by the use of conformally deposited metal oxide blocking layers *J. Am. Chem. Soc.* **125** 475–82
[8] Ito S, Kitamura T, Wada Y and Yanagida S 2003 Facile fabrication of mesoporous TiO2 electrodes for dye solar cells: chemical modification and repetitive coating *Sol. Energy Mater. Sol. Cells* **76** 3–13
[9] Emeji I C, Ama O M, Aigbe U O, Khoele K, Osifo P O and Ray S S 2020 Electrochemical cells *Eng Mater* **414** 65–84
[10] Mukhokosi E P, Tenywa S, Botha N L, Azizi S, Seopelad M and Maaza M 2025 Green synthesis of CuO nanoparticles from cucurbita maxima leaf extract; a platinum free counter electrode for dye sensitized solar cells *J Niger Soc Phys Sci* **7** 2309
[11] Sowmiya M, Selvam K and Shivakumar M S 2025 Sustainable fabrication of zinc oxide nanoparticles using Secamone emetica leaf extract: Biological and environmental applications *J Nat Pestic Res* **12** 100122
[12] Jiang C Y, Sun X W, Lo G Q, Kwong D L and Wang J X 2007 Improved dye-sensitized solar cells with A ZnO-nanoflower photoanode *Appl. Phys. Lett.* **90** 2005–8
[13] Jadhav V, Dhanwate Y, Raut P, Shinde S, Sawant R and Bhagare A 2025 Efficient photocatalytic methylene blue dye degradation from green—synthesized silver—doped iron oxide (Ag@Fe2O3) nanostructures *Discov Nano* **20** 66
[14] Cui L, Thuong P T, Lee H S, Ndinteh D T, Mbafor J T, Fomum Z T and Oh W K 2008 Flavanones from the stem bark of erythrina abyssinica *Bioorganic Med Chem* **16** 10356–62
[15] Giannozzi P *et al* 2020 Quantum ESPRESSO toward the exascale *J. Chem. Phys.* **152** 154105
[16] Burke K, Perdew J P and Ernzerhof M 1997 Why the generalized gradient approximation works and how to go beyond it *Int. J. Quantum Chem.* **61** 287–93
[17] Bashyal K, Pyles C K, Afroosheh S, Lamichhane A and Zayak A T 2018 Empirical optimization of DFT + U and HSE for the band structure of ZnO *J. Phys. Condens. Matter* **30** 065501
[18] Dudarev S L, Botton G A, Savrasov S Y, Humphreys C J and Sutton A P 1998 Electron-energy-loss spectra and the structural stability of nickel oxide: An LSDA+U study *Phys. Rev. B* **57** 1505–9
[19] Mukhokosi E P, Mohammed T, Loyce N, Botha N L, Maaza M and Velauthapillai D 2024 Co-sensitization effect of chlorophyll and anthocyanin on optical absorption properties and power conversion efficiency of dye-sensitized solar cells *J. Korean Phys. Soc.* **84** 858–69

[20] Mukhokosi E P, Maaza M, Tibenkana M and Botha N L 2023 Optical absorption and photoluminescence properties of Cucurbita maxima dye adsorption on TiO2 nanoparticles *Mater. Res. Express* **10** 046203
[21] Molefe F V, Koao L F, Dejene B F and Swart H C 2015 Phase formation of hexagonal wurtzite ZnO through decomposition of Zn(OH) 2 at various growth temperatures using CBD method *Opt Mater (Amst)* **46** 292–8
[22] Awan S U, Hasanain S K, Rashid J, Hussain S, Shah S A, Hussain M Z, Rafique M, Aftab M and Khan R 2018 Structural, optical, electronic and magnetic properties of multiphase ZnO/Zn(OH)2/ZnO2 nanocomposites and hexagonal prism shaped ZnO nanoparticles synthesized by pulse laser ablation in Heptanes *Mater. Chem. Phys.* **211** 510–21
[23] Suresh R, Ponnuswamy V and Mariappan R 2013 Effect of annealing temperature on the microstructural, optical and electrical properties of CeO 2 nanoparticles by chemical precipitation method *Appl. Surf. Sci.* **273** 457–64
[24] Hwang J S and Jung K Y 2021 Effect of calcination temperature and Ti substitution on optical properties of (Fe,Cr)2O3cool black pigment prepared by spray pyrolysis *RSC Adv.* **12** 72–7
[25] Sarkar J, Ghosh M, Mukherjee A, Chattopadhyay D and Acharya K 2014 Biosynthesis and safety evaluation of ZnO nanoparticles *Bioprocess. Biosyst. Eng.* **37** 165–71
[26] Balogun S W, James O O, Sanusi Y K and Olayinka O H 2020 Green synthesis and characterization of zinc oxide nanoparticles using bashful (Mimosa pudica), leaf extract: a precursor for organic electronics applications *SN Appl Sci* **2** 1–8
[27] Fakhari S, Jamzad M and Kabiri Fard H 2019 Green synthesis of zinc oxide nanoparticles: a comparison *Green Chem. Lett. Rev.* **12** 19–24
[28] Raoufi D 2013 Synthesis and photoluminescence characterization of ZnO nanoparticles *J. Lumin.* **134** 213–9
[29] Hong R Y, Li J H, Chen L L, Liu D Q, Li H Z, Zheng Y and Ding J 2009 Synthesis, surface modification and photocatalytic property of ZnO nanoparticles *Powder Technol.* **189** 426–32
[30] Hong R Y, Qian J Z and Cao J X 2006 Synthesis and characterization of PMMA grafted ZnO nanoparticles *Powder Technol.* **163** 160–8
[31] Azizi S, Mohamad R, Bahadoran A, Bayat S, Rahim R A, Ariff A and Saad W Z 2016 Effect of annealing temperature on antimicrobial and structural properties of bio-synthesized zinc oxide nanoparticles using flower extract of Anchusa italica *J Photochem Photobiol B Biol* **161** 441–9
[32] Zare E, Pourseyedi S, Khatami M and Darezereshki E 2017 Simple biosynthesis of zinc oxide nanoparticles using nature's source, and it's in vitro bio-activity *J. Mol. Struct.* **1146** 96–103
[33] Davis K, Yarbrough R, Froeschle M, White J and Rathnayake H 2019 Band gap engineered zinc oxide nanostructures: via a sol-gel synthesis of solvent driven shape-controlled crystal growth *RSC Adv.* **9** 14638–48
[34] Vittal R and Ho K C 2017 Zinc oxide based dye-sensitized solar cells: a review *Renew. Sustain. Energy Rev.* **70** 920–35
[35] Abdullah H, Omar A, Razali M Z and Yarmo M A 2014 Photovoltaic properties of ZnO photoanode incorporating with CNTs for dye-sensitized solar cell application *Ionics (Kiel)* **20** 1023–30
[36] Sanjay P, Isaivani I, Deepa K, Madhavan J and Senthil S 2019 The preparation of dye sensitized solar cells using natural dyes extracted from Phytolacca icosandra and Phyllanthus reticulatus with ZnO as photoanode *Mater. Lett.* **244** 142–6
[37] Shaat S, Zayed H, Musleh H, Shurrab N, Issa A, Asad J and Al Dahoudi N 2017 Inexpensive organic dyes-sensitized zinc oxide nanoparticles photoanode for solar cells devices *J Photonics Energy* **7** 025504
[38] Esakki E S, Sarathi R, Sundar S M and Devi L R 2021 Fabrication of dye sensitized solar cells using ixora macrothyrsa *Mater. Today Proc.* **47** 2182–7
[39] Chandiran A K, Abdi-Jalebi M, Nazeeruddin M K and Grätzel M 2014 Analysis of electron transfer properties of ZnO and TiO2 photoanodes for dye-sensitized solar cells *ACS Nano* **8** 2261–8
[40] Apaolaza A, Richard D and Tejerina M 2020 Experimental and *ab initio* study of the structural and optical properties of ZnO coatings: performance of the DFT+U approach *Process Appl Ceram* **14** 362–71
[41] Harun K, Salleh N A, Deghfel B, Yaakob M K and Mohamad A A 2020 DFT + U calculations for electronic, structural, and optical properties of ZnO wurtzite structure: a review *Results Phys* **16** 102829
[42] Duong Q-V 2024 Investigation of structural and electronic properties of ZnO using first principle calculations *HPU2 J Sci Nat Sci Technol* **3** 78–87
[43] Khan W, Betzler S B, Šipr O, Ciston J, Blaha P, Scheu C and Minar J 2016 Theoretical and experimental study on the optoelectronic properties of Nb3O7(OH) and Nb2O5 photoelectrodes *J. Phys. Chem. C* **120** 23329–38
[44] Berrezoug H I, Merad A E, Zerga A and Hassoun Z S 2014 Ab-initio calculations of structural, electronic, and dielectric properties of ZnO *North African Workshop on Dielectic Materials for Photovoltaic Systems (NAWDMPV)* 1–5